

18 **ABSTRACT**

19 The global radiative effect of brown carbon (BrC) remains highly uncertain. BrC's
20 photobleaching, which significantly affects its radiative effect, has been still poorly constrained.
21 This study investigates and compares photobleaching rates of laboratory-synthesized secondary
22 BrC (aq-BrC), biomass burning-derived BrC (b-BrC), and ambient PM_{2.5}-derived BrC (p-BrC) to
23 illustrate the variability in BrC photobleaching kinetics from different types of BrC reported in
24 prior studies. Our results reveal a source dependence in BrC photobleaching rates. The highest
25 photobleaching rate constant (k_{BrC}) is observed for aq-BrC ($1.13 \pm 0.08 \text{ h}^{-1}$), followed by p-BrC
26 ($0.12 \pm 0.02 \text{ h}^{-1}$) and b-BrC ($0.05 \pm 0.01 \text{ h}^{-1}$), indicating the stable light-absorption capacity of b-
27 BrC in the atmosphere. Integration of these rate constants with data derived from previous studies
28 highlighted the differences in photobleaching behaviors among BrC from different sources. The
29 OH oxidation of imidazole-2-carboxaldehyde (2-IC) and methylglyoxal oligomers, nitrophenols
30 (including phenols), and lignin derivatives governs the photobleaching of aq-BrC, p-BrC, and b-
31 BrC, respectively. The high k_{BrC} of aq-BrC is attributed to the high reactivity of the chain structures
32 in 2-IC and methylglyoxal oligomers. In contrast, the highly conjugated structures of lignin
33 derivatives in b-BrC impart stability against OH oxidation, resulting in a low k_{BrC} . Our findings
34 reveal the significant differences in the photobleaching behavior of BrC originated from different
35 sources, underscoring the crucial need to account for source differences in assessments of BrC's
36 global radiative forcing effect.

37

38 1. Introduction

39 Brown carbon (BrC) is a significant contributor to atmospheric warming (Saleh, 2020; Chung et al., 2012;
40 Brown et al., 2021) and Earth's radiative budget (Bond, 2001; Kirchstetter et al., 2004; Wang et al., 2018; Wang
41 et al., 2022) due to its ultraviolet-visible (UV-Vis) light absorption. The BrC's direct radiative effect (DRE),
42 accounting for 20%–40% of total DRE caused by light-absorbing carbonaceous aerosols (Heald et al., 2014; Jo
43 et al., 2016; Saleh et al., 2015; Wang et al., 2018; Wang et al., 2014), remains highly uncertainty. BrC with global
44 average DRE values varying from +0.03 to +0.57 W/m² is considered as the least understood warming agents in
45 the atmosphere (Zhang et al., 2020; Zeng et al., 2020; Corr et al., 2012).

46 BrC comprises abundant chemically reactive species that react readily with atmospheric reactive gases and
47 radicals (Aiona et al., 2017; Fleming et al., 2020; Hems et al., 2021; Liu et al., 2020), modifying its light-
48 absorption properties. Both laboratory experiments (Borduas-Dedekind et al., 2019; Fleming et al., 2019; Hems
49 and Abbatt, 2018; Hems et al., 2020; Schnitzler and Abbatt, 2018; Schnitzler et al., 2022) and field campaigns
50 (Dasari et al., 2019; Qiu et al., 2024; Wang et al., 2014; Xu et al., 2024; Zeng et al., 2020) consistently found
51 that BrC's photochemical aging process reduced its mass absorption coefficient (MAC), which is also known as
52 photobleaching. In current models, the evaluation of BrC photobleaching on its radiative forcing effect mainly
53 depends on the temporal decline in BrC's light-absorption capacity (Schnitzler et al., 2022; Wang et al., 2018;
54 Xu et al., 2024), i.e., the photobleaching rate, which is substantial variability across different laboratory
55 experiments and field observations. Notably, BrC generated from aqueous-phase reactions often exhibits
56 negligible absorbance in the UV-Vis range after less than 2 hours of radiation (Aiona et al., 2017). Field
57 observations reveal that atmospheric BrC undergoes a MAC reduction exceeding 60% after 1 day of sunlight
58 exposure (Müller et al., 2023; Qiu et al., 2024). In comparison, over the same 1 day of solar radiation, the
59 reduction in the MAC of BrC derived from biomass burning is much lower than atmospheric BrC (Fan et al.,
60 2019; Fleming et al., 2020; Müller et al., 2023; Wong et al., 2019). Accurately determining BrC's photobleaching
61 rate is paramount for quantifying the impact of BrC photobleaching on its radiative forcing effect in models.

62 Furthermore, BrC's chemical composition fundamentally governs its photochemical reactivity (Hems et al.,
63 2021; Hems and Abbatt, 2018; Dalton and Nizkorodov, 2021; Liu et al., 2025), thereby modulating its
64 photobleaching rate. However, the relationship between changes in BrC's molecular composition and light
65 absorption properties during the photobleaching is still poorly constrained. This knowledge gap leads to
66 significant uncertainty in evaluating the evolution of BrC's light absorption capacity during atmospheric
67 transportation. For instance, BrC emitted from biomass burning has been observed to retain strong absorption
68 after several days of transport to the Arctic (Yue et al., 2022). In contrast, model simulations estimate BrC is
69 nearly complete photobleaching over this timescale (Wang et al., 2018; Xu et al., 2024), which contradicts the
70 observational evidence. Elucidating the linkage between BrC molecular composition and photobleaching rates
71 would improve the accuracy of global-scale assessments of BrC's dynamic light absorption properties during
72 long-range transport.

73 In this work, we performed photochemical aging experiments on three types of BrC under identical,
74 controlled conditions, including synthesized by aqueous phase reaction (referred to "aq-BrC"), and extracted

75 from ambient (referred to “p-BrC”, where “p” denotes particulate) and biomass burning (referred to “b-BrC”)
76 PM_{2.5} samples. Compared to previous studies, this work systematically investigated the differences in
77 photobleaching kinetics among various types of BrC under identical environmental conditions. We combine this
78 with high-resolution mass spectrometry (HRMS) analysis to establish a mechanistic link between the observed
79 divergent BrC photobleaching rates and the evolution of key molecular chromophores. In addition, we quantify
80 the contribution of the OH oxidation pathway across all BrC types. These findings aim to provide essential
81 parameters and a mechanistic basis for improving the representation of BrC photochemical aging in climate
82 models.

83 **2. Methodology**

84 **2.1 Preparation of BrC**

85 Methylglyoxal (MG, 40 wt%, Merck) and ammonium sulfate (AS, 98%, Aladdin) solutions (1 mol/L) was
86 mixed in darkness at room temperature for 2 h (pH 3.7–4.2) (Yang et al., 2024) to generate aq-BrC. Residual
87 MG/AS were removed by solid-phase extraction (SPE) (Lin et al., 2010; Wang et al., 2017). The eluent was
88 dried under gentle stream of ultrapure N₂ (>99.99%) and reconstituted in ultrapure water (18.2 MΩ·cm).
89 Previous studies have confirmed that MG is one of the most abundant dicarbonyl species in the atmosphere (Gu
90 et al., 2025; Fu et al., 2008), which is produced by primary emissions and oxidation of volatile organic
91 compounds (VOCs). Considering that MG exhibit a tendency to partition into aqueous aerosols and cloud
92 droplets in the atmosphere (Laskin et al., 2015), therefore, the secondary BrC generated by the aqueous-phase
93 reaction between MG and AS is representative as aq-BrC.

94 PM_{2.5} samples emitted from corn straw combustion in household stoves was collected on quartz fiber filters
95 (25 × 20 cm, Whatman) using a high-volume sampler (TH-1000H, Wuhan Tianhong; 1.05 m³/min). Corn straw
96 is recognized as a typical and common domestic biomass fuel in China, constituting approximately 40.0% of the
97 total output from the agricultural products and has an estimated annual production of about 295 million tons.
98 Therefore, PM_{2.5} emitted from corn straw combustion was selected as typical biomass burning aerosols in this
99 work. Figure S1 shows a schematic of sample collection process of biomass burning PM_{2.5} samples, and Table
100 S1 summarizes the concentrations of organic carbon (OC), element carbon (EC), the concentration of total
101 organic carbon (TOC) of each sample. This approach closely represents real-world biomass burning emissions
102 (Chen et al., 2019; Shan et al., 2017). For each sample, background aerosols were collected for 1 hour both
103 before to and after the sampling period.

104 We selected five atmospheric PM_{2.5} samples collected at Peking University Changping Campus (40°8'N,
105 116°6'E) from 15 December 2020 to 15 January 2021 to extract p-BrC. Table S2 summarizes the sampling time
106 and average PM_{2.5} mass concentrations during sampling of each sample. All samples were collected using a
107 high-volume sampler with the flow rate of 1.05 m³/min. Gaseous pollutants, PM_{2.5} mass concentrations, non-
108 refractory submicron particles (NR-PM₁) chemical composition, and meteorology were monitored (Figure S2;
109 details in Table S3).

110 For those PM_{2.5} samples, twenty 1.5-cm² filter sections were ultrasonically extracted in LC-MS grade

111 methanol (Merck Inc.) for twice (20 min) to extract p-BrC and b-BrC. Extracts were dried gentle stream of
112 ultrapure N₂ (>99.99%) and redissolved in ultrapure water.

113 **2.2 Laboratory aqueous-phase photochemical aging setup**

114 Photochemical aging experiments were conducted in a temperature-controlled (20 ± 0.1 °C) chamber,
115 equipped with 20 UV bulbs (40 W; λ_{max} = 370 nm). The TOC of all BrC solutions were adjusted to 50 mgC/L.
116 BrC solutions were irradiated in quartz bottles (10 mL) with added H₂O₂ (30 wt%, Alaadin) to generate OH
117 radicals. Steady-state OH concentrations ([OH]_{ss}) were quantified via pseudo-first-order decay of benzoic acid
118 (methods detailed in Section S1 in Supplementary Information) (Hems and Abbatt, 2018). The average [OH]_{ss}
119 was (3.17 ± 0.47) × 10⁻¹⁴ mol/L, slightly below typical cloud water maxima.

120 The transition from laboratory experimental illumination to actual solar radiation was applied by calculating
121 the ratio between laboratory and actual spectral flux densities following the identical calculation approach used
122 in our previous study (Qiu et al., 2024). Briefly, the scaling factor can be approximated as the ratio between the
123 integrated spectral flux densities of two different light sources. The spectral flux densities of the UV bulbs used
124 in this work and the 24-hour average Beijing solar spectrum at 300 m above sea level were integrated from 360
125 nm to 380 nm (see Section S2 in Supplementary Information for detail). The 24-hour average Beijing solar
126 spectrum was simulated using the Tropospheric Ultraviolet and Visible Radiation model (Table S4), and Figure
127 S3 shows the comparison between calculated and measured radiation spectrum. The calculated scaling factor in
128 this work is 3.86 (Qiu et al., 2024). Samples were collected at 0, 2, 4, 8, and 16 hours of equivalent solar radiation.

129 Furthermore, a series of control experiments were performed under H₂O₂ free and dark conditions. In both
130 cases, the same BrC solutions (50 mgC/L TOC) were used for different types of BrC. The former consisted of
131 16 hours of radiation in the absence of H₂O₂. The dark experiments involved storing the solutions in complete
132 darkness for an identical period (16 hours) to account for any non-photochemical changes.

133 These experiments were configured to delineate the contributions of different pathways to BrC
134 photobleaching. The H₂O₂ added photochemical aging experiments elucidates the synergistic effect of OH
135 oxidation, direct BrC photolysis, and other light-independent reactions occur in dark conditions. The H₂O₂ free
136 experiments considered the sole contribution of the direct photolytic pathway. In addition, the dark control
137 experiments served to investigate any potential influence of chemical reactions in dark conditions on the BrC's
138 light-absorption capacity.

139 **2.3 Light-absorption properties and molecular composition analysis of BrC**

140 UV-Vis absorption spectra (250–700 nm) were recorded using a spectrophotometer (UV-1780, Shimadzu
141 Inc.). MAC normalized absorption to TOC concentrations. In eq.(1), $A_{10}^{abs}(\lambda)$, b , and c denotes the measured
142 base-10 absorbance, optical path length (1 cm), and measured TOC, respectively.

$$143 \quad \text{MAC}(\lambda) = \frac{A_{10}^{abs}(\lambda) \times \ln(10)}{b \times c} \quad (1)$$

144 BrC's molecular composition was analyzed via HRMS (Orbitrap FusionTM TribridTM, Thermo Scientific)

145 with electrospray ionization (ESI) in negative mode (ESI(-); m/z 70–700). Samples were directly injected into
146 HRMS at a flow rate of 10 $\mu\text{L}/\text{min}$. Triplicate analyses ensured reproducibility, with only peaks detected in all
147 replicates retained for assignment. Molecular formulas ($\text{C}_x\text{H}_y\text{O}_z\text{N}_w\text{S}_n$; $x = 1\text{--}90$, $y = 1\text{--}200$, $z = 0\text{--}20$, $w = 0\text{--}3$,
148 $n = 0\text{--}1$) were assigned with m/z error lower than ± 0.005 Da. The H/C, O/C, N/C, and S/C atom ratios for each
149 assigned formula were constrained to 0.3–3.0, 0–3.0, 0–0.5, and 0–2.0, respectively (Wang et al., 2017). Signal-
150 intensity-weighted average elemental compositions (eq.(2)), O/C atom ratios, and N/C atom ratios (eq.(3)) were
151 calculated as:

$$152 \quad Y = \frac{\sum_i x_i Y_i}{\sum_i x_i}, \text{ where } Y = \text{C, H, O, N, and S} \quad (2)$$

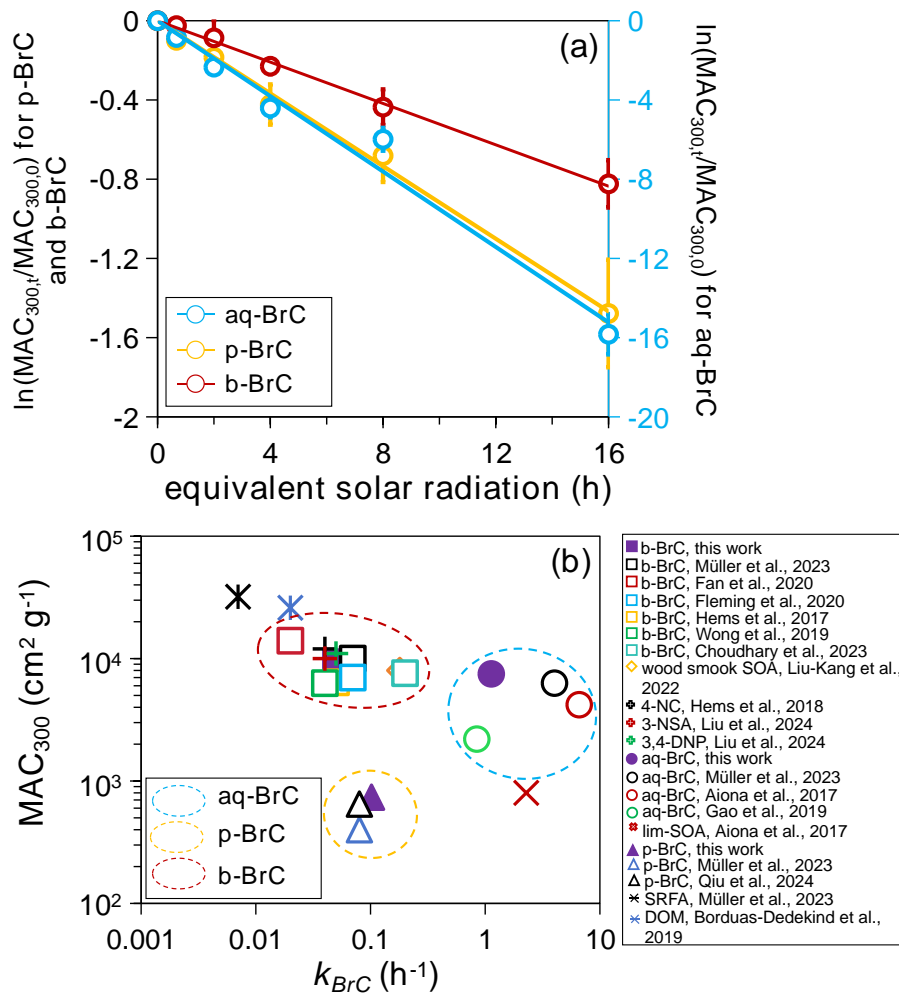
$$153 \quad Y/Z = \frac{\sum_i x_i Y_i}{\sum_i x_i Z_i}, \text{ where } Y/Z = \text{O/C or N/C} \quad (3)$$

154 where x_i in eqs. (2) and (3) indicated the signal-intensity-weighted factor.

155 **3. Results and Discussion**

156 **3.1 Quantification and Comparison of BrC Photobleaching Rates**

157 Given that BrC's light-absorption properties at shorter wavelengths are a better indicator of its
158 photobleaching kinetics (Aiona et al., 2017), we focused our analysis on the variation in the MAC at 300 nm
159 (MAC_{300}). The measured MAC_{300} of aq-BrC, p-BrC, and b-BrC is $(7.32 \pm 0.89) \times 10^3 \text{ cm}^2 \text{ g}^{-1}$, $(7.38 \pm 0.83) \times$
160 $10^2 \text{ cm}^2 \text{ g}^{-1}$, and $(9.44 \pm 0.71) \times 10^3 \text{ cm}^2 \text{ g}^{-1}$, respectively. Figure 1(a) shows the overall decay of MAC_{300} for
161 different BrC types, plotted as the natural logarithm of the ratio ($\ln(\text{MAC}_{300,t}/\text{MAC}_{300,0})$) versus irradiation hours.
162 The left axis of Figure 1(a) shows the variation in $\ln(\text{MAC}_{300,t}/\text{MAC}_{300,0})$ for p-BrC and b-BrC, while the right
163 axis denotes this variation for aq-BrC. Here, $\text{MAC}_{300,t}$ and $\text{MAC}_{300,0}$ denote the MAC_{300} after t hours of
164 irradiation and its initial value, respectively. The observed linear decay demonstrates that BrC undergoes
165 photobleaching regardless of its source. The aq-BrC has been almost completely bleached in the initial 2 hours.
166 The MAC_{300} decreased by 77.2% after 16 hours of radiation. In comparison, for b-BrC, the MAC_{300} only
167 decreased by 56.1%. Even after extending to 32 hours of radiation, b-BrC still kept strong light-absorption
168 capacity (see Figure S4). The differences in the variation in MAC_{300} for different types of BrC demonstrate that
169 aq-BrC undergoes rapid photobleaching in the presence of solar radiation, while b-BrC exhibits stable light-
170 absorption capacity during photobleaching.



171
 172 **Figure 1** (a) Variations in the $\ln(\text{MAC}_{300,t}/\text{MAC}_{300,0})$ of aq-BrC (blue plots, right axis), p-BrC (yellow plots, left
 173 axis), and b-BrC (red plots, left axis) as a function of radiation hours. Blue, yellow, and red lines indicate fitted
 174 k_{BrC} of aq-BrC, p-BrC, and b-BrC. Error bars represent one standard deviation of datapoints derive from three
 175 (aq-BrC and b-BrC) or five (p-BrC) parallel experiments. (b) The relationship between MAC_{300} and calculated
 176 k_{BrC} of different types of BrC in this work and other studies. 4-NC, 3-NSA, 3,4-DNP, SRFA, and DOM represents
 177 4-nitrocateol, 3-mitrosalicylic acid, 3,4-dinitrophenol, Suwannee River fulvic acid standard, and dissolved
 178 organic matters, respectively. Blue, yellow, and red circles marked aq-BrC (including BrC generated via
 179 aldehyde-amine condensation reactions), p-BrC, and b-BrC (including representative compounds emitted from
 180 biomass burning). The exact MAC_{300} values are obtained from figures in corresponding literatures, and k_{BrC} are
 181 calculated based on the MAC_{300} and hours of radiation.

182 The liner decline in $\ln(\text{MAC}_{300,t}/\text{MAC}_{300,0})$ indicates that BrC photobleaching fitted the pseudo-first order
 183 kinetic, which was represented by the negative slope of $\ln(\text{MAC}_{300,t}/\text{MAC}_{300,0})$ vs. radiation hours:

184
$$\text{MAC}_{300,t} = \text{MAC}_{300,0} \times \exp(-k_{BrC}t) \quad (4)$$

185 where k_{BrC} is the overall photobleaching rate constant. The calculated k_{BrC} of aq-BrC, p-BrC, and b-BrC were
 186 $(1.13 \pm 0.08) \text{ hour}^{-1}$, $(0.12 \pm 0.02) \text{ hour}^{-1}$, and $(0.05 \pm 0.01) \text{ hour}^{-1}$, respectively. Correspondingly, the lifetime of

187 BrC (τ_{BrC} , indicated by BrC's absorption decreased to 1/e of its initial value) (Schnitzler et al., 2022) were 1.05
188 hours, 10.91 hours, and 19.16 hours, respectively. Longer τ_{BrC} of b-BrC indicates its absorption largely retains
189 during atmospheric transportation process. This order-of-magnitude difference in k_{BrC} among three BrC types,
190 quantified under comparable conditions, highlights a fundamental source dependency that cannot be attributed
191 to environmental condition variability. This clear difference necessitates a molecular-level explanation, which
192 we pursue by examining the dominant bleaching pathway and the underlying chemical composition.

193 Figure 1(b) presents a comparison of MAC_{300} versus overall k_{BrC} for BrC from various sources, including
194 data from this study and other studies (data and references in Table S5). Based on their sources, we classified
195 aq-BrC (including BrC generated via aldehyde-amine condensation reactions), p-BrC, and b-BrC (including
196 representative compounds emitted from biomass burning) in three different clusters. Our results are comparable
197 to those of previous studies. The characteristic of aq-BrC is strong absorption, rapid photobleaching. This
198 demonstrates that the light-absorption capacity of BrC generated by secondary atmospheric aqueous phase
199 reactions (De Haan et al., 2017) decrease rapidly in the presence of solar radiation. In stark contrast, b-BrC
200 shows strong absorption but slow photobleaching, implying its stable strong absorption in the atmosphere. p-
201 BrC exhibits weak absorption and slow photobleaching, which has also been observed in different urban areas,
202 including Eastern China (Qiu et al., 2024), India (Dasari et al., 2019), Northern Europe (Müller et al., 2023), and
203 the United States (Chen et al., 2021). It is noteworthy that p-BrC contains a mixture of primary and secondary
204 BrC that is challenging to separate quantitatively. However, from molecular composition and solar radiation
205 during sampling, p-BrC is considered to be predominantly of primary emissions. Herein, we further analyzed
206 the molecular composition of p-BrC following the non-target analysis approach used in our previous study (Qiu
207 et al., 2024), more details were described in Section S3 in Supplementary Information. Figure S5 shows the
208 molecular composition and relevant solar radiation during sampling, which is represented by the 75th percentile
209 solar radiation (Rad_{75}). Low Rad_{75} showed limited photochemical aging prior to analysis, and high mass fraction
210 of nitrophenols proved the dominate role of primary emission for p-BrC.

211 Having investigated the differences in overall photobleaching rates across different BrC types, we further
212 elucidated the underlying mechanisms by assessing the contribution of each photobleaching pathway. Previous
213 studies suggest that BrC photobleaching occurs via three different pathways, including direct photolysis, OH
214 oxidation, and other light-independent reactions occur in dark conditions (Gao and Zhang, 2019; Liu-Kang et
215 al., 2022; Wong et al., 2019). Choudhary et al. (2023) (Choudhary et al., 2023) have demonstrated that in the
216 presence of H_2O_2 , the overall k_{BrC} can be expressed as a linear sum of the pseudo first-order effective
217 photobleaching rate constant due to OH oxidation ($k_{BrC,OH}$), BrC direct photolysis ($k_{BrC,pho}$), and other light-
218 independent reactions occur in dark conditions ($k_{BrC,ctrl}$), see eq. (5):

$$219 \quad k_{BrC} = k_{BrC,OH} + k_{BrC,pho} + k_{BrC,ctrl} \quad (5)$$

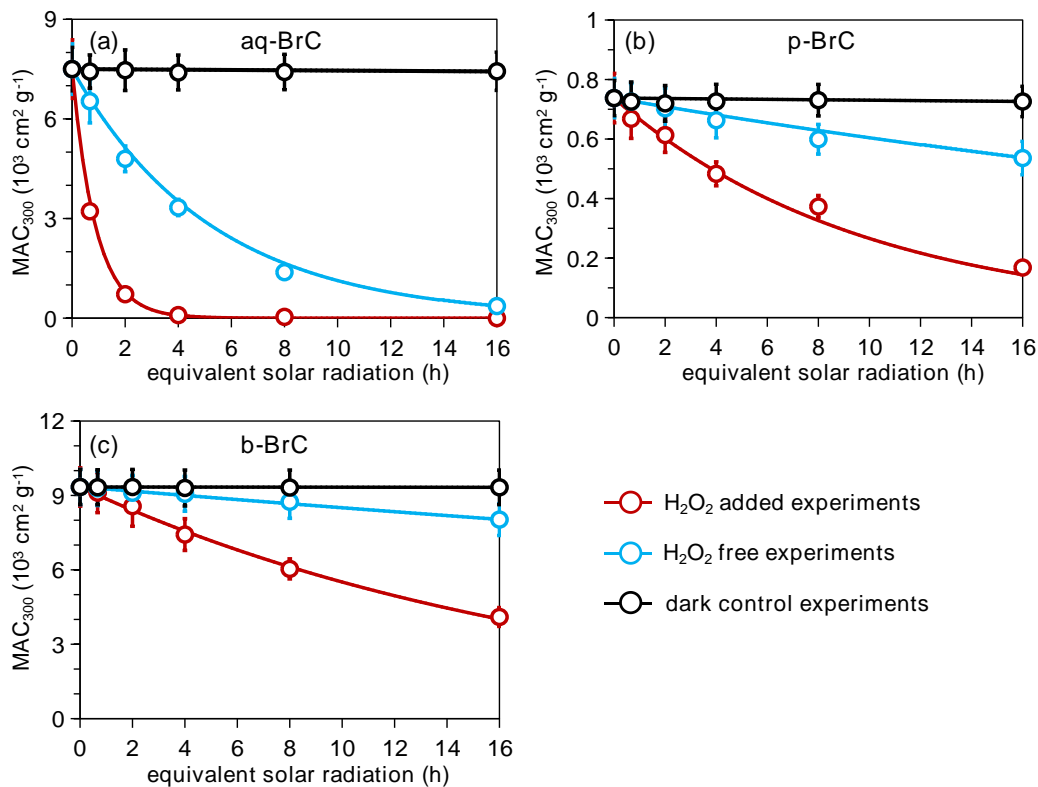
220 The $k_{BrC,pho}$ and $k_{BrC,ctrl}$ are derived from the pseudo-first-order decay of MAC_{300} in H_2O_2 free experiments
221 and dark control experiments, respectively, using the calculation approach identical to eq. (4) and the
222 experimental procedures detailed in Section 2.2. Therefore, although $k_{BrC,OH}$ cannot be measured directly, it can
223 be indirectly determined by calculating the difference between the overall k_{BrC} and the sum of $k_{BrC,pho}$ (from H_2O_2
224 free experiments) and $k_{BrC,ctrl}$ (from dark control experiments).

Table 1 The $k_{BrC,ctrl}$, $k_{BrC,pho}$, and $k_{BrC,OH}$ for different BrC types

BrC type	$k_{BrC,ctrl}$	$k_{BrC,pho}$	$k_{BrC,OH}$
aq-BrC	$(0.004 \pm 0.002) \text{ h}^{-1}$	$(0.19 \pm 0.03) \text{ h}^{-1}$	$(0.94 \pm 0.06) \text{ h}^{-1}$
p-BrC	$(0.007 \pm 0.001) \text{ h}^{-1}$	$(0.02 \pm 0.005) \text{ h}^{-1}$	$(0.08 \pm 0.02) \text{ h}^{-1}$
b-BrC	$(0.006 \pm 0.002) \text{ h}^{-1}$	$(0.01 \pm 0.004) \text{ h}^{-1}$	$(0.04 \pm 0.01) \text{ h}^{-1}$

226 Figure 2 displays the variations in MAC_{300} in photochemical aging experiments (with H_2O_2 , red line,
 227 representing the synergistic effect of OH oxidation, direct BrC photolysis, and other light-independent reactions
 228 occur in dark conditions), H_2O_2 free experiments (blue line, representing the contribution of BrC direct
 229 photolysis), and dark control experiments (black line, representing the contribution of other light-independent
 230 reactions occur in dark conditions). It is noted that for dark control experiments, the x-axis denotes the time the
 231 BrC solution is kept under dark conditions. Table 1 summarizes the $k_{BrC,ctrl}$, $k_{BrC,pho}$, and $k_{BrC,OH}$ for different BrC
 232 types. Specifically, MAC_{300} variations were negligible in dark controls, rendering the calculated $k_{BrC,ctrl}$ was close
 233 to 0. For all BrC types, $k_{BrC,pho}$ was substantially lower than $k_{BrC,OH}$. The overwhelming contribution of $k_{BrC,OH}$
 234 (over 80% of k_{BrC}) unambiguously identifies OH oxidation as the dominant mechanism governing BrC
 235 photobleaching. The dominate role of OH oxidation in BrC photobleaching have been also proved in several
 236 previous studies (Choudhary et al., 2023; Hems and Abbatt, 2018; Zhao et al., 2015), this work provide
 237 quantitative and comparative evidence regardless of BrC types. Consequently, the observed differences in k_{BrC}
 238 among different types of BrC can be fundamentally attributed to the molecular-composition-dependent reactivity
 239 of BrC components toward OH radicals. Hence, understanding the underlying molecular composition that
 240 determine a BrC molecule's susceptibility to this OH oxidation.

241 It is important to note that the laboratory-synthesized aq-BrC represents a simplified chemical system.
 242 While it provides a clear mechanistic understanding of rapid photobleaching driven by BrC chromophores with
 243 high chemical reactivity, real atmospheric aqueous-phase processes involve more complex precursors and
 244 mixtures, yielding secondary BrC with different photobleaching kinetics. Nevertheless, the dominate role of OH
 245 oxidation established in this work, which provides a critical lens through which to interpret the slower
 246 photobleaching rates of the more complex ambient (p-BrC) and biomass burning (b-BrC) samples.



247

248 **Figure 2** The variations in MAC₃₀₀ in photochemical aging experiments (with H₂O₂, red line, representing the
 249 synergistic effect of OH oxidation, direct BrC photolysis, and other light-independent reactions occur in dark
 250 conditions), H₂O₂ free experiments (blue line, representing the variation in MAC₃₀₀ contributed by BrC direct
 251 photolysis), and dark control experiments (black line, representing the variation in MAC₃₀₀ contributed by other
 252 light-independent reactions occur in dark conditions) for (a) aq-BrC, (b) p-BrC, and (c) b-BrC, respectively. For
 253 dark control experiments (black line), the x-axis represents the time the BrC solution is kept in the absence of
 254 light.

255 3.2 Chemical investigation of different BrC photobleaching rates

256 To elucidating the differences in BrC photobleaching rates, we investigated BrC's molecular composition
 257 before and after photobleaching, which was represented by BrC's molecular composition after 16 hours of
 258 radiation.

259 Table 2 summarizes the signal-intensity-weighted average elemental compositions, molecular weights, O/C
 260 ratios, and N/C ratios of different types of BrC before and after 16 hours of radiation. The observed decrease in
 261 average molecular weights upon photobleaching across all BrC types, alongside an elevated O/C ratio, points to
 262 the production of more oxidized, lower-mass species. Additionally, we found the mass concentrations of low-
 263 molecular-weight organic acids (formic acid, acetic acid, and oxalic acid; see Figure S6) significantly increased
 264 with longer radiation hours, demonstrating carbon backbone fragmentation (Borduas-Dedekind et al., 2019).
 265 Figure S7 demonstrates that more products with lower C atom numbers are detected after photobleaching, further
 266 proves the carbon backbone fragmentation. Considering OH oxidation dominates BrC photobleaching, the

267 molecular-level evolution aligns with OH-mediated degradation pathways (Hems et al., 2020; Qiu et al., 2024;
 268 Liu et al., 2025): (i) electrophilic addition to unsaturated bonds (like C=C bonds) and (ii) subsequent carbon
 269 backbone fragmentation.

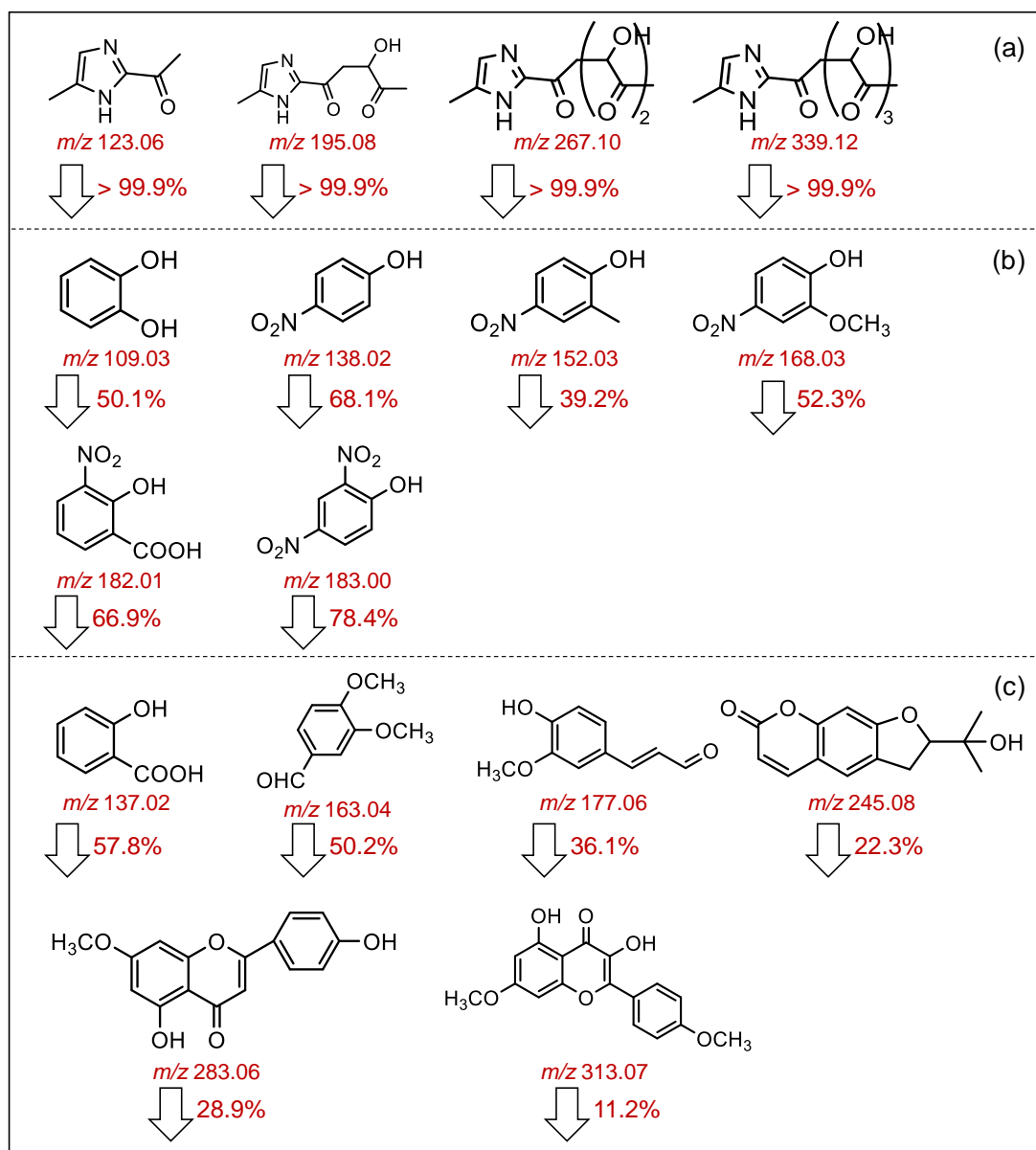
270 In addition, the reduced N/C atom ratios (Table 2) further confirmed degradation of N-containing
 271 compounds, which are key UV-Vis absorbers contributing significantly to BrC absorption (Lin et al., 2017; Wang
 272 et al., 2019; Zeng et al., 2021; Li et al., 2025). The formation of compounds with higher oxidation states and the
 273 degradation of N-containing compounds reduce the conjugation degrees of BrC, diminishing $\pi \rightarrow \pi^*$ electronic
 274 transitions and weakening light-absorption capacity.

275 **Table 2** Variations in the signal-intensity-weighted average elemental compositions, molecular weights,
 276 O/C ratios, and N/C ratios of different types of BrC before and after photobleaching

aq-BrC	elemental composition	molecular weight	O/C	N/C
before	C _{8.94} H _{10.22} O _{4.64} N _{1.33}	210.36	0.52	0.15
after	C _{8.22} H _{10.17} O _{4.66} N _{1.07}	198.35	0.57	0.12
p-BrC	elemental composition	molecular weight	O/C	N/C
before	C _{7.88} H _{8.38} O _{2.47} N _{2.13} S _{0.65}	193.08	0.31	0.28
after	C _{7.21} H _{9.17} O _{2.52} N _{1.82} S _{0.68}	183.25	0.35	0.25
b-BrC	elemental composition	molecular weight	O/C	N/C
before	C _{15.92} H _{16.68} O _{6.05} N _{1.18} S _{0.31}	330.96	0.38	0.08
after	C _{15.42} H _{16.92} O _{6.11} N _{1.07} S _{0.41}	327.82	0.40	0.07

277 Subsequently, we determined representative BrC chromophores relate to the photobleaching of different
 278 types of BrC based on the following three criteria. Firstly, we calculated the differential HRMS spectra of
 279 different types of BrC before and after photobleaching (Figure S8). These peaks with negative intensities (> 3
 280 times the signal-to-noise ratio) denote species consumed after photobleaching. Secondly, these candidate species
 281 were cross-compared to identify compounds that were highly characteristic of each specific source. Lastly,
 282 tandem HRMS (HRMS²) analysis was adopted to determine the chemical structure of selected BrC
 283 chromophores.

284 In this work, the photooxidation of MG and imidazole-2-carboxaldehyde (2-IC) oligomers (Aiona et al.,
 285 2017) with formula C_{3n}H_{4n}N₂O_{2n-3} (n = 2-5; including *m/z* 123.06, 195.08, 267.10, and 339.12), phenols and
 286 nitrophenols (Hems and Abbatt, 2018; Magalhães et al., 2017) (including *m/z* 109.03, 138.02, 152.03, 168.03,
 287 182.01, and 183.00), and lignin derivatives (Fleming et al., 2020) (including *m/z* 137.02, 163.04, 245.08, 283.06,
 288 and 313.07) were identified as the dominant reactions in the photobleaching of aq-BrC, p-BrC, and b-BrC,
 289 respectively. Compounds identified as products after photobleaching for aq-BrC, p-BrC, and b-BrC are
 290 respectively summarized in Tables S6-S8. It is acknowledged that secondary BrC comprises a wide variety of
 291 compounds formed through different pathways. While phenols and nitrophenols identified here can themselves
 292 be secondary products, their markedly slower photobleaching rate (compared to the MG/AS-derived aq-BrC in
 293 this work) highlights the substantial kinetic diversity within the broader secondary BrC. This further reinforces
 294 that the molecular architecture, rather than the primary or secondary classification, is the fundamental
 295 determinant of BrC photochemical stability.



296

297 **Figure 3** The chemical structures of (a) MG and 2-IC oligomers detected in aq-BrC; (b) phenols and nitrophenols
 298 detected in p-BrC, and (c) lignin derivatives detected in b-BrC. The detected m/z for these compounds are marked
 299 under their structures. The ratios of decline in signal intensities for these compounds after 16 hours of radiation
 300 are indicated next to the bottom arrows.

301 Figure 3 displays the chemical structures of these MG and 2-IC oligomers, phenols and nitrophenols, and
 302 lignin derivatives, as well as the declines in their signal intensities after 16 hours of radiation. Variations in
 303 HRMS signal intensities represent the changes in the mass concentrations, though specific mass concentrations
 304 cannot be derived. Figure 3(a) illustrates the predominant molecular species and the corresponding decline in
 305 MG and 2-IC oligomers during the photobleaching of aq-BrC. Following photobleaching, these oligomers
 306 became undetectable (signal-to-noise ratio < 3), experiencing a reduction in signal intensity of >99.9% (Figure

307 3(a)). This observation is consistent with the nearly complete bleaching of aq-BrC. The high reactivity of the
308 chain structures of MG and 2-IC oligomers with OH radicals (Aiona et al., 2017) explains the elevated k_{BrC} value
309 observed for aq-BrC.

310 As shown in Figure 3(b), a greater number of electron-withdrawing substituents on the benzene ring
311 correlates with a more significant decline of signal intensity after photobleaching. For instance, 2-methyl-4-
312 nitrophenol (m/z 152.03), which bears an electron-donating methyl group in addition to the electron-withdrawing
313 nitro substituent present in 4-nitrophenol (m/z 138.02), demonstrates a comparatively lower signal attenuation
314 of 39.2% after photobleaching, whereas 4-nitrophenol exhibits a signal decrease of 68.1%. The electron-
315 withdrawing substituents exert both inductive and resonance effects, effectively diminishing the electron density
316 of the π -system of the aromatic ring. This electron-deficient state enhances the susceptibility of these species to
317 nucleophilic attack by OH radicals, thereby facilitating their photooxidation and contributing to the observed
318 photobleaching behavior. However, the reactivity of these species remains lower than that of MG and 2-IC
319 oligomers, which explains lower k_{BrC} for p-BrC compares to aq-BrC.

320 In comparison, the signal intensities of the majority of lignin derivatives only decreased by below 50%,
321 corresponding to the lowest k_{BrC} for b-BrC (Figure 3(c)). Specifically, nodakenetin and flavonoids (m/z 245.08,
322 283.06, and 313.07) exhibit highly stabilized molecular structures, wherein the aromatic rings conjugated with
323 oxygen-containing heterocyclic moieties significantly reduce their chemical reactivity, resulting in low k_{BrC} for
324 b-BrC. The chemical stability of lignin derivatives has been also proved by previous laboratory experiment
325 (Wong et al., 2019). However, studies found that levoglucosan, which is an important component in biomass
326 burning aerosols, may be oxidized by OH radicals and therefore slow down the reaction of other BrC
327 chromophores reacting with OH (Bai et al., 2013; Zhao et al., 2014). In this work, the same TOC mass
328 concentrations (50 mg/L) across all BrC types provides equal total potential OH sinks, making the observed
329 order-of-magnitude difference in k_{BrC} more likely attributable to the reactivity of the chromophores themselves
330 rather than solely to differences in competitor abundance. Additionally, the identified lignin derivatives exhibited
331 low signal decay percentages despite being exposed to the same $[OH]_{ss}$ as the highly reactive BrC chromophores.
332 Hence, it is expected that the chemical stability of lignin derivative leads to the low k_{BrC} for b-BrC.

333 We noted that the exact variation in the mass concentration of compounds shown in Figure 3 were not
334 derived in this work. Ultra-high performance liquid chromatography (UHPLC)-HRMS analysis using standards
335 or surrogate standards should be adopted to obtain the mass concentration of these compounds. However, this
336 work aims to comparatively track the changes in molecular composition for each specific BrC type before and
337 after photobleaching. While absolute quantification is not feasible based on HRMS analysis, the relative changes
338 in signal intensity for a given compound are comparable within the same sample matrix. Therefore, the variation
339 in signal intensity for a specific m/z can be reliably interpreted as a corresponding change in its relative mass
340 concentration.

341 In addition, while the species highlighted in Figure 3 were rigorously selected as representative and reactive
342 chromophores through the differential screening and structural identification process described above, we fully
343 acknowledge that our analysis may not capture all potential BrC chromophores. Limitations in analytical
344 sensitivity, chromatographic separation, and the chemical complexity of BrC result in several BrC chromophores,

345 particularly those at low concentrations or with poor ionization efficiency, might not be detected or their changes
346 fully characterized. Therefore, while the reported decay percentages for the identified species are robust, the
347 total BrC photobleaching likely involves contributions from additional chromophores not specifically tracked
348 here.

349 **4. Conclusion and Atmospheric Implication**

350 This work quantifies the k_{BrC} for three different types of BrC and demonstrates that their order-of-magnitude
351 differences (aq-BrC > p-BrC > b-BrC) originate from distinct molecular susceptibilities to OH-driven oxidation
352 through controlled comparative experiments. While the source dependency of BrC photobleaching has been
353 suggested, our study mechanistically establishes the linkage between BrC photobleaching kinetics and molecular
354 composition. Specifically, rapid photobleaching of aq-BrC is governed by the high OH reactivity of MG and 2-
355 IC oligomers; in comparison, the remarkable stability of b-BrC is attributed to resilient, conjugated aromatic
356 systems in lignin derivatives. For p-BrC, an intermediate k_{BrC} was observed, consistent with the oxidation
357 kinetics of nitrophenolic chromophores. Critically, we show that OH oxidation accounts for >80% of the total
358 photobleaching across all sources, identifying it as the dominant and unifying chemical pathway under aqueous
359 conditions.

360 These quantified, source-dependent k_{BrC} values and their molecular-level changes emphasizes the
361 necessitate explicit consideration of source variability when evaluating BrC's radiative effect. Current models
362 often assume constant k_{BrC} based on simplified representative compounds or field data (Hems and Abbatt, 2018;
363 Schnitzler et al., 2022; Wang et al., 2018), yet substantial discrepancies exist. For instance, the reported k_{BrC}
364 values differ by approximately an order of magnitude between field observations and laboratory simulations
365 (Schnitzler et al., 2022; Wang et al., 2018). Spatiotemporal heterogeneity in BrC sources (Xiong et al., 2022)
366 (fossil fuel/biomass combustion, secondary formation) drives global regional variations in k_{BrC} . We should
367 acknowledge that though source-dependent BrC photobleaching rates are essential in assessing BrC's global
368 DRE, the impact of environmental conditions like temperature and relative humidity are also decisive (Schnitzler
369 et al., 2022).

370 In addition, the low k_{BrC} for b-BrC explains unexpectedly high BrC absorption in remote regions (e.g., the
371 Arctic). Field data confirm biomass burning contributes 57% of Arctic BrC while < 10% for secondary BrC (Yue
372 et al., 2022). Previous studies have confirmed that biomass burning aerosols contains substantial amounts of
373 lignin derivatives (Wong et al., 2019), which exhibit strong light-absorbing properties and chemical stability in
374 OH oxidation. Therefore, during the long-range transport (Zhang et al., 2025), b-BrC is expected to retain strong
375 absorption, leading to enhancement of the aerosol DRE over large spatial scales. On a global scale, one major
376 source of b-BrC is wildfire events (Wang et al., 2025; Shen et al., 2024; Bond et al., 2004). With the increasing
377 frequency of wildfires (Yue et al., 2013; Hurteau et al., 2014; Cunningham et al., 2024; Jain et al., 2022), the
378 emission of b-BrC is expected to rise correspondingly. In all, b-BrC would exert a significant influence on BrC's
379 global radiative effect.

380 **Data Availability**

381 The data used in this study is available upon request from the corresponding author (zhijunwu@pku.edu.cn).

382 **Author Contributions**

383 Y.Q. and Z.W. designed this work. Y.Q., T.Q., Y.G., and D.L. collected and analyzed the measurement data.
384 Y.Q., T.Q., Y.L., and R.M. analyzed UHPLC-MS data. Z.W. and M.H. edited the manuscript. All authors have
385 read and agreed to submit this manuscript.

386 **Funding**

387 This work is funded by National Natural Science Foundation of China – Youth Program (42507137), China
388 Postdoctoral Science Foundation (2025M771267), and the National Key Research and Development Program
389 of China (2022YFC3701000, Task 4).

390 **Competing Interests**

391 The authors declare that they have no conflict of interest.

392 **Acknowledgements**

393 This research has been supported by the National Natural Science Foundation of China (grant no.
394 42507137), Chinese Postdoctoral Science Foundation (grant no. 2025M771267), the National Key Research and
395 Development Program of China (grant no. 2022YFC3701000, Task 4).

396

397 **References**

- 398 Aiona, P. K., Lee, H. J., Leslie, R., Lin, P., Laskin, A., Laskin, J., and Nizkorodov, S. A.: Photochemistry of
399 Products of the Aqueous Reaction of Methylglyoxal with Ammonium Sulfate, *ACS Earth and Space Chemistry*, 1,
400 522-532, <https://doi.org/10.1021/acsearthspacechem.7b00075>, 2017.
- 401 Bai, J., Sun, X., Zhang, C., Xu, Y., and Qi, C.: The OH-initiated atmospheric reaction mechanism and kinetics
402 for levoglucosan emitted in biomass burning, *Chemosphere*, 93, 2004-2010,
403 <https://doi.org/10.1016/j.chemosphere.2013.07.021>, 2013.
- 404 Bond, T. C.: Spectral dependence of visible light absorption by carbonaceous particles emitted from coal
405 combustion, *Geophysical Research Letters*, 28, 4075-4078, <https://doi.org/10.1029/2001GL013652>, 2001.
- 406 Bond, T. C., Streets, D. G., Yarber, K. F., Nelson, S. M., Woo, J.-H., and Klimont, Z.: A technology-based global
407 inventory of black and organic carbon emissions from combustion, *Journal of Geophysical Research: Atmospheres*,
408 109, <https://doi.org/10.1029/2003JD003697>, 2004.
- 409 Borduas-Dedekind, N., Ossola, R., David, R. O., Boynton, L. S., Weichlinger, V., Kanji, Z. A., and McNeill, K.:
410 Photomineralization mechanism changes the ability of dissolved organic matter to activate cloud droplets and to
411 nucleate ice crystals, *Atmospheric Chemistry and Physics*, 19, 12397-12412, [https://doi.org/10.5194/acp-19-12397-](https://doi.org/10.5194/acp-19-12397-2019)
412 [2019](https://doi.org/10.5194/acp-19-12397-2019), 2019.
- 413 Brown, H., Liu, X., Pokhrel, R., Murphy, S., Lu, Z., Saleh, R., Mielonen, T., Kokkola, H., Bergman, T., Myhre,
414 G., Skeie, R. B., Watson-Paris, D., Stier, P., Johnson, B., Bellouin, N., Schulz, M., Vakkari, V., Beukes, J. P., van Zyl,
415 P. G., Liu, S., and Chand, D.: Biomass burning aerosols in most climate models are too absorbing, *Nature*
416 *Communications*, 12, 277, <https://doi.org/10.1038/s41467-020-20482-9>, 2021.
- 417 Chen, L.-W. A., Chow, J. C., Wang, X., Cao, J., Mao, J., and Watson, J. G.: Brownness of Organic Aerosol over
418 the United States: Evidence for Seasonal Biomass Burning and Photobleaching Effects, *Environmental Science &*
419 *Technology*, 55, 8561-8572, <https://doi.org/10.1021/acs.est.0c08706>, 2021.
- 420 Chen, Q., Sun, H., Wang, J., Shan, M., Yang, X., Deng, M., Wang, Y., and Zhang, L.: Long-life type — The
421 dominant fraction of EPFRs in combustion sources and ambient fine particles in Xi'an, *Atmos. Environ.*, 219, 117059,
422 <https://doi.org/10.1016/j.atmosenv.2019.117059>, 2019.
- 423 Choudhary, V., Roson, M. L., Guo, X., Gautam, T., Gupta, T., and Zhao, R.: Aqueous-phase photochemical
424 oxidation of water-soluble brown carbon aerosols arising from solid biomass fuel burning, *Environmental Science:*
425 *Atmospheres*, 3, 816-829, <https://doi.org/10.1039/D2EA00151A>, 2023.
- 426 Chung, C. E., Ramanathan, V., and Decremmer, D.: Observationally constrained estimates of carbonaceous aerosol
427 radiative forcing, *Proceedings of the National Academy of Sciences USA*, 109, 11624-11629,
428 <https://doi.org/10.1073/pnas.1203707109>, 2012.
- 429 Corr, C. A., Hall, S. R., Ullmann, K., Anderson, B. E., Beyersdorf, A. J., Thornhill, K. L., Cubison, M. J., Jimenez,
430 J. L., Wisthaler, A., and Dibb, J. E.: Spectral absorption of biomass burning aerosol determined from retrieved single

431 scattering albedo during ARCTAS, *Atmospheric Chemistry and Physics*, 12, 10505-10518,
432 <https://doi.org/10.5194/acp-12-10505-2012>, 2012.

433 Cunningham, C. X., Williamson, G. J., and Bowman, D. M. J. S.: Increasing frequency and intensity of the most
434 extreme wildfires on Earth, *Nature Ecology & Evolution*, 8, 1420-1425, <https://doi.org/10.1038/s41559-024-02452-2>,
435 2024.

436 Dalton, A. B., and Nizkorodov, S. A.: Photochemical Degradation of 4-Nitrocatechol and 2,4-Dinitrophenol in a
437 Sugar-Glass Secondary Organic Aerosol Surrogate, *Environmental Science & Technology*, 55, 14586-14594,
438 <https://doi.org/10.1021/acs.est.1c04975>, 2021.

439 Dasari, S., Andersson, A., Bikkina, S., Holmstrand, H., Budhavant, K., Satheesh, S., Asmi, E., Kesti, J., Backman,
440 J., Salam, A., Bisht, D. S., Tiwari, S., Hameed, Z., and Gustafsson, Ö.: Photochemical degradation affects the light
441 absorption of water-soluble brown carbon in the South Asian outflow, *Science Advances*, 5, eaau8066,
442 <https://doi.org/10.1126/sciadv.aau8066>, 2019.

443 De Haan, D. O., Hawkins, L. N., Welsh, H. G., Pednekar, R., Casar, J. R., Pennington, E. A., de Loera, A., Jimenez,
444 N. G., Symons, M. A., Zauscher, M., Pajunoja, A., Caponi, L., Cazaunau, M., Formenti, P., Gratien, A., Pangui, E.,
445 and Doussin, J.-F.: Brown Carbon Production in Ammonium- or Amine-Containing Aerosol Particles by Reactive
446 Uptake of Methylglyoxal and Photolytic Cloud Cycling, *Environmental Science & Technology*, 51, 7458-7466,
447 <https://doi.org/10.1021/acs.est.7b00159>, 2017.

448 Fan, X., Yu, X., Wang, Y., Xiao, X., Li, F., Xie, Y., Wei, S., Song, J., and Peng, P. a.: The aging behaviors of
449 chromophoric biomass burning brown carbon during dark aqueous hydroxyl radical oxidation processes in laboratory
450 studies, *Atmospheric Environment*, 205, 9-18, <https://doi.org/10.1016/j.atmosenv.2019.02.039>, 2019.

451 Fleming, L. T., Ali, N. N., Blair, S. L., Roveretto, M., George, C., and Nizkorodov, S. A.: Formation of Light-
452 Absorbing Organosulfates during Evaporation of Secondary Organic Material Extracts in the Presence of Sulfuric
453 Acid, *ACS Earth and Space Chemistry*, 3, 947-957, <https://doi.org/10.1021/acsearthspacechem.9b00036>, 2019.

454 Fleming, L. T., Lin, P., Roberts, J. M., Selimovic, V., Yokelson, R., Laskin, J., Laskin, A., and Nizkorodov, S. A.:
455 Molecular composition and photochemical lifetimes of brown carbon chromophores in biomass burning organic
456 aerosol, *Atmospheric Chemistry and Physics*, 20, 1105-1129, <https://doi.org/10.5194/acp-20-1105-2020>, 2020.

457 Fu, T.-M., Jacob, D. J., Wittrock, F., Burrows, J. P., Vrekoussis, M., and Henze, D. K.: Global budgets of
458 atmospheric glyoxal and methylglyoxal, and implications for formation of secondary organic aerosols, *Journal of*
459 *Geophysical Research: Atmospheres*, 113, <https://doi.org/10.1029/2007JD009505>, 2008.

460 Gao, Y., and Zhang, Y.: Optical properties investigation of the reactions between methylglyoxal and
461 glycine/ammonium sulfate, *Spectrochimica Acta Part A: Molecular and Biomolecular Spectroscopy*, 215, 112-121,
462 <https://doi.org/10.1016/j.saa.2019.02.087>, 2019.

463 Gu, J., Dutta, S., Sioud, S., Go, B. R., Maity, B., Cavallo, L., Zhang, R., and Chan, C. K.: Photoinduced
464 Transformation in Glyoxal- and Methylglyoxal-Ammonium Solutions: Role of Photolysis and Photosensitization,
465 *Environmental Science & Technology*, 59, 16628-16640, <https://doi.org/10.1021/acs.est.5c04889>, 2025.

466 Heald, C. L., Ridley, D. A., Kroll, J. H., Barrett, S. R. H., Cady-Pereira, K. E., Alvarado, M. J., and Holmes, C.
467 D.: Contrasting the direct radiative effect and direct radiative forcing of aerosols, *Atmospheric Chemistry and Physics*,
468 14, 5513-5527, <https://doi.org/10.5194/acp-14-5513-2014>, 2014.

469 Hems, R. F., and Abbatt, J. P. D.: Aqueous Phase Photo-oxidation of Brown Carbon Nitrophenols: Reaction
470 Kinetics, Mechanism, and Evolution of Light Absorption, *ACS Earth and Space Chemistry*, 2, 225-234,
471 <https://doi.org/10.1021/acsearthspacechem.7b00123>, 2018.

472 Hems, R. F., Schnitzler, E. G., Bastawrous, M., Soong, R., Simpson, A. J., and Abbatt, J. P. D.: Aqueous
473 Photoreactions of Wood Smoke Brown Carbon, *ACS Earth and Space Chemistry*, 4, 1149-1160,
474 <https://doi.org/10.1021/acsearthspacechem.0c00117>, 2020.

475 Hems, R. F., Schnitzler, E. G., Liu-Kang, C., Cappa, C. D., and Abbatt, J. P. D.: Aging of Atmospheric Brown
476 Carbon Aerosol, *ACS Earth and Space Chemistry*, 5, 722-748, <https://doi.org/10.1021/acsearthspacechem.0c00346>,
477 2021.

478 Hurteau, M. D., Westerling, A. L., Wiedinmyer, C., and Bryant, B. P.: Projected Effects of Climate and
479 Development on California Wildfire Emissions through 2100, *Environmental Science & Technology*, 48, 2298-2304,
480 <https://doi.org/10.1021/es4050133>, 2014.

481 Jain, P., Castellanos-Acuna, D., Coogan, S. C. P., Abatzoglou, J. T., and Flannigan, M. D.: Observed increases in
482 extreme fire weather driven by atmospheric humidity and temperature, *Nature Climate Change*, 12, 63-70,
483 <https://doi.org/10.1038/s41558-021-01224-1>, 2022.

484 Jo, D. S., Park, R. J., Lee, S., Kim, S. W., and Zhang, X.: A global simulation of brown carbon: implications for
485 photochemistry and direct radiative effect, *Atmospheric Chemistry and Physics*, 16, 3413-3432,
486 <https://doi.org/10.5194/acp-16-3413-2016>, 2016.

487 Kirchstetter, T. W., Novakov, T., and Hobbs, P. V.: Evidence that the spectral dependence of light absorption by
488 aerosols is affected by organic carbon, *Journal of Geophysical Research: Atmospheres*, 109,
489 <https://doi.org/10.1029/2004JD004999>, 2004.

490 Laskin, A., Laskin, J., and Nizkorodov, S. A.: Chemistry of Atmospheric Brown Carbon, *Chemical Reviews*, 115,
491 4335-4382, <https://doi.org/10.1021/cr5006167>, 2015.

492 Li, Y., Fu, T.-M., Yu, J. Z., Zhang, A., Yu, X., Ye, J., Zhu, L., Shen, H., Wang, C., Yang, X., Tao, S., Chen, Q., Li,
493 Y., Li, L., Che, H., and Heald, C. L.: Nitrogen dominates global atmospheric organic aerosol absorption, *Science*, 387,
494 989-995, <https://doi.org/10.1126/science.adr4473>, 2025.

495 Lin, P., Huang, X.-F., He, L.-Y., and Zhen Yu, J.: Abundance and size distribution of HULIS in ambient aerosols
496 at a rural site in South China, *Journal of Aerosol Science*, 41, 74-87, <https://doi.org/10.1016/j.jaerosci.2009.09.001>,
497 2010.

498 Lin, P., Bluvshstein, N., Rudich, Y., Nizkorodov, S. A., Laskin, J., and Laskin, A.: Molecular Chemistry of
499 Atmospheric Brown Carbon Inferred from a Nationwide Biomass Burning Event, *Environmental Science &*
500 *Technology*, 51, 11561-11570, <https://doi.org/10.1021/acs.est.7b02276>, 2017.

501 Liu-Kang, C., Gallimore, P. J., Liu, T., and Abbatt, J. P. D.: Photoreaction of biomass burning brown carbon
502 aerosol particles, *Environmental Science: Atmospheres*, 2, 270-278, <https://doi.org/10.1039/d1ea00088h>, 2022.

503 Liu, D., He, C., Schwarz, J. P., and Wang, X.: Lifecycle of light-absorbing carbonaceous aerosols in the
504 atmosphere, *npj Climate and Atmospheric Science*, 3, 40, <https://doi.org/10.1038/s41612-020-00145-8>, 2020.

505 Liu, Y., Huang, R.-J., Lin, C., Yuan, W., Li, Y. J., Zhong, H., Yang, L., Wang, T., Huang, W., Xu, W., Huang, D.
506 D., and Huang, C.: Nitrate-Photolysis Shortens the Lifetimes of Brown Carbon Tracers from Biomass Burning,
507 *Environmental Science & Technology*, 59, 640-649, <https://doi.org/10.1021/acs.est.4c06123>, 2025.

508 Magalhães, A. C. O., Esteves da Silva, J. C. G., and Pinto da Silva, L.: Density Functional Theory Calculation of
509 the Absorption Properties of Brown Carbon Chromophores Generated by Catechol Heterogeneous Ozonolysis, *ACS*
510 *Earth and Space Chemistry*, 1, 353-360, <https://doi.org/10.1021/acsearthspacechem.7b00061>, 2017.

511 Müller, S., Giorio, C., and Borduas-Dedekind, N.: Tracking the Photomineralization Mechanism in Irradiated
512 Lab-Generated and Field-Collected Brown Carbon Samples and Its Effect on Cloud Condensation Nuclei Abilities,
513 *ACS Environmental Au*, 3, 164-178, <https://doi.org/10.1021/acsenvironau.2c00055>, 2023.

514 Qiu, Y., Qiu, T., Wu, Z., Liu, Y., Fang, W., Man, R., Liu, Y., Wang, J., Meng, X., Chen, J., Liang, D., Guo, S., and
515 Hu, M.: Observational Evidence of Brown Carbon Photobleaching in Urban Atmosphere at Molecular Level,
516 *Environmental Science and Technology Letters*, 11, 1032-1039, <https://doi.org/10.1021/acs.estlett.4c00647>, 2024.

517 Saleh, R., Marks, M., Heo, J., Adams, P. J., Donahue, N. M., and Robinson, A. L.: Contribution of brown carbon
518 and lensing to the direct radiative effect of carbonaceous aerosols from biomass and biofuel burning emissions, *Journal*
519 *of Geophysical Research: Atmospheres*, 120, 10,285-210,296, <https://doi.org/10.1002/2015JD023697>, 2015.

520 Saleh, R.: From Measurements to Models: Toward Accurate Representation of Brown Carbon in Climate
521 Calculations, *Current Pollution Reports*, 6, 90-104, <https://doi.org/10.1007/s40726-020-00139-3>, 2020.

522 Schnitzler, E. G., and Abbatt, J. P. D.: Heterogeneous OH oxidation of secondary brown carbon aerosol,
523 *Atmospheric Chemistry and Physics*, 18, 14539-14553, <https://doi.org/10.5194/acp-18-14539-2018>, 2018.

524 Schnitzler, E. G., Gerrebos, N. G. A., Carter, T. S., Huang, Y., Heald, C. L., Bertram, A. K., and Abbatt, J. P. D.:
525 Rate of atmospheric brown carbon whitening governed by environmental conditions, *Proceedings of the National*
526 *Academy of Sciences*, 119, e2205610119, <https://doi.org/10.1073/pnas.2205610119>, 2022.

527 Shan, M., Carter, E., Baumgartner, J., Deng, M., Clark, S., Schauer, J. J., Ezzati, M., Li, J., Fu, Y., and Yang, X.:
528 A user-centered, iterative engineering approach for advanced biomass cookstove design and development, *Environ.*
529 *Res. Lett.*, 12, 095009, [10.1088/1748-9326/aa804f](https://doi.org/10.1088/1748-9326/aa804f), 2017.

530 Shen, Y., Pokhrel, R. P., Sullivan, A. P., Levin, E. J. T., Garofalo, L. A., Farmer, D. K., Permar, W., Hu, L., Toohey,
531 D. W., Campos, T., Fischer, E. V., and Murphy, S. M.: Understanding the mechanism and importance of brown carbon
532 bleaching across the visible spectrum in biomass burning plumes from the WE-CAN campaign, *Atmospheric*
533 *Chemistry and Physics*, 24, 12881-12901, <https://doi.org/10.5194/acp-24-12881-2024>, 2024.

534 Wang, Q., Zhou, Y., Ma, N., Zhu, Y., Zhao, X., Zhu, S., Tao, J., Hong, J., Wu, W., Cheng, Y., and Su, H.: Review
535 of Brown Carbon Aerosols in China: Pollution Level, Optical Properties, and Emissions, *Journal of Geophysical*

536 Research: Atmospheres, 127, e2021JD035473, <https://doi.org/10.1029/2021JD035473>, 2022.

537 Wang, X., Heald, C. L., Ridley, D. A., Schwarz, J. P., Spackman, J. R., Perring, A. E., Coe, H., Liu, D., and Clarke,
538 A. D.: Exploiting simultaneous observational constraints on mass and absorption to estimate the global direct radiative
539 forcing of black carbon and brown carbon, *Atmospheric Chemistry and Physics*, 14, 10989-11010,
540 <https://doi.org/10.5194/acp-14-10989-2014>, 2014.

541 Wang, X., Heald, C. L., Liu, J., Weber, R. J., Campuzano-Jost, P., Jimenez, J. L., Schwarz, J. P., and Perring, A.
542 E.: Exploring the observational constraints on the simulation of brown carbon, *Atmospheric Chemistry and Physics*,
543 18, 635-653, <https://doi.org/10.5194/acp-18-635-2018>, 2018.

544 Wang, X., Chakrabarty, R. K., Schwarz, J. P., Murphy, S. M., Levin, E. J. T., Howell, S. G., Guo, H., Campuzano-
545 Jost, P., and Jimenez, J. L.: Dark brown carbon from biomass burning contributes to significant global-scale positive
546 forcing, *One Earth*, 8, 101205, <https://doi.org/10.1016/j.oneear.2025.101205>, 2025.

547 Wang, Y., Hu, M., Lin, P., Guo, Q., Wu, Z., Li, M., Zeng, L., Song, Y., Zeng, L., Wu, Y., Guo, S., Huang, X., and
548 He, L.: Molecular Characterization of Nitrogen-Containing Organic Compounds in Humic-like Substances Emitted
549 from Straw Residue Burning, *Environmental Science & Technology*, 51, 5951-5961,
550 <https://doi.org/10.1021/acs.est.7b00248>, 2017.

551 Wang, Y., Hu, M., Lin, P., Tan, T., Li, M., Xu, N., Zheng, J., Du, Z., Qin, Y., Wu, Y., Lu, S., Song, Y., Wu, Z.,
552 Guo, S., Zeng, L., Huang, X., and He, L.: Enhancement in Particulate Organic Nitrogen and Light Absorption of
553 Humic-Like Substances over Tibetan Plateau Due to Long-Range Transported Biomass Burning Emissions,
554 *Environmental Science & Technology*, 53, 14222-14232, <https://doi.org/10.1021/acs.est.9b06152>, 2019.

555 Wong, J. P. S., Tsagkaraki, M., Tsiodra, I., Mihalopoulos, N., Violaki, K., Kanakidou, M., Sciare, J., Nenes, A.,
556 and Weber, R. J.: Atmospheric evolution of molecular-weight-separated brown carbon from biomass burning,
557 *Atmospheric Chemistry and Physics*, 19, 7319-7334, <https://doi.org/10.5194/acp-19-7319-2019>, 2019.

558 Xiong, R., Li, J., Zhang, Y., Zhang, L., Jiang, K., Zheng, H., Kong, S., Shen, H., Cheng, H., Shen, G., and Tao,
559 S.: Global brown carbon emissions from combustion sources, *Environmental Science and Ecotechnology*, 12, 100201,
560 <https://doi.org/10.1016/j.ese.2022.100201>, 2022.

561 Xu, L., Lin, G., Liu, X., Wu, C., Wu, Y., and Lou, S.: Constraining Light Absorption of Brown Carbon in China
562 and Implications for Aerosol Direct Radiative Effect, *Geophysical Research Letters*, 51, e2024GL109861,
563 <https://doi.org/10.1029/2024GL109861>, 2024.

564 Yang, L., Huang, R.-J., Yuan, W., Huang, D. D., and Huang, C.: pH-Dependent Aqueous-Phase Brown Carbon
565 Formation: Rate Constants and Implications for Solar Absorption and Atmospheric Photochemistry, *Environmental*
566 *Science & Technology*, 1236-1243, <https://doi.org/10.1021/acs.est.3c07631>, 2024.

567 Yue, S., Zhu, J., Chen, S., Xie, Q., Li, W., Li, L., Ren, H., Su, S., Li, P., Ma, H., Fan, Y., Cheng, B., Wu, L., Deng,
568 J., Hu, W., Ren, L., Wei, L., Zhao, W., Tian, Y., Pan, X., Sun, Y., Wang, Z., Wu, F., Liu, C.-Q., Su, H., Penner, J. E.,
569 Pöschl, U., Andreae, M. O., Cheng, Y., and Fu, P.: Brown carbon from biomass burning imposes strong circum-Arctic
570 warming, *One Earth*, 5, 293-304, <https://doi.org/10.1016/j.oneear.2022.02.006>, 2022.

571 Yue, X., Mickley, L. J., Logan, J. A., and Kaplan, J. O.: Ensemble projections of wildfire activity and
572 carbonaceous aerosol concentrations over the western United States in the mid-21st century, *Atmospheric*
573 *Environment*, 77, 767-780, <https://doi.org/10.1016/j.atmosenv.2013.06.003>, 2013.

574 Zeng, L., Zhang, A., Wang, Y., Wagner, N. L., Katich, J. M., Schwarz, J. P., Schill, G. P., Brock, C., Froyd, K. D.,
575 Murphy, D. M., Williamson, C. J., Kupc, A., Scheuer, E., Dibb, J., and Weber, R. J.: Global Measurements of Brown
576 Carbon and Estimated Direct Radiative Effects, *Geophysical Research Letters*, 47, e2020GL088747,
577 <https://doi.org/10.1029/2020GL088747>, 2020.

578 Zeng, Y., Ning, Y., Shen, Z., Zhang, L., Zhang, T., Lei, Y., Zhang, Q., Li, G., Xu, H., Ho, S. S. H., and Cao, J.:
579 The Roles of N, S, and O in Molecular Absorption Features of Brown Carbon in PM_{2.5} in a Typical Semi-Arid
580 Megacity in Northwestern China, *Journal of Geophysical Research: Atmospheres*, 126, e2021JD034791,
581 <https://doi.org/10.1029/2021JD034791>, 2021.

582 Zhang, Q., Wang, Y., Xiao, Q., Geng, G., Davis, S. J., Liu, X., Yang, J., Liu, J., Huang, W., He, C., Luo, B.,
583 Martin, R. V., Brauer, M., Randerson, J. T., and He, K.: Long-range PM_{2.5} pollution and health impacts from the 2023
584 Canadian wildfires, *Nature*, <https://doi.org/10.1038/s41586-025-09482-1>, 2025.

585 Zhang, X., Chen, S., Kang, L., Yuan, T., Luo, Y., Alam, K., Li, J., He, Y., Bi, H., and Zhao, D.: Direct Radiative
586 Forcing Induced by Light-Absorbing Aerosols in Different Climate Regions Over East Asia, *Journal of Geophysical*
587 *Research: Atmospheres*, 125, e2019JD032228, <https://doi.org/10.1029/2019JD032228>, 2020.

588 Zhao, R., Mungall, E. L., Lee, A. K. Y., Aljawhary, D., and Abbatt, J. P. D.: Aqueous-phase photooxidation of
589 levoglucosan – a mechanistic study using aerosol time-of-flight chemical ionization mass spectrometry
590 (Aerosol ToF-CIMS), *Atmospheric Chemistry and Physics*, 14, 9695-9706, <https://doi.org/10.5194/acp-14-9695-2014>,
591 2014.

592 Zhao, R., Lee, A. K. Y., Huang, L., Li, X., Yang, F., and Abbatt, J. P. D.: Photochemical processing of aqueous
593 atmospheric brown carbon, *Atmospheric Chemistry and Physics*, 15, 6087-6100, [https://doi.org/10.5194/acp-15-6087-](https://doi.org/10.5194/acp-15-6087-2015)
594 [2015](https://doi.org/10.5194/acp-15-6087-2015), 2015.

595